Mon. Not. R. Astron. Soc. **299,** 1146–1158 (1998)

Microturbulence in O supergiants

K. C. Smith and I. D. Howarth
Department of Physics & Astronomy, University College London, Gower Street, London WC1E 6BT

Accepted 1998 May 25. Received 1998 May 19; in original form 1998 January 16

ABSTRACT

We investigate the role of classical microturbulence in the non-LTE He I/He II line formation problem for luminous O-type stars. We find that the shapes and strengths of certain saturated He I lines, in particular the triplets λλ4471, 4713 and the singlet λ4921, are sensitive to microturbulent velocities in excess of $5\,\mathrm{km\,s^{-1}}$. Weaker lines, including most of the He I singlets, are effectively independent of this parameter, as are the Fowler series He II lines λλ4199, 4541, 5411. We show that this behaviour is due to interaction between direct line-broadening effects in the radiative transfer, and indirect changes in the atmospheric structure and the populations of absorbing states. Using an analysis of high-resolution, high signal-to-noise ratio observations of the O9.7 supergiant HD 152003 as an illustrative example, we show how the introduction of microturbulence in non-LTE models allows consistent fits to be obtained for *all* blue-region He I lines – including the strong triplets λλ4026, 4713, 4471 – at an assumed solar helium abundance, thereby offering a resolution to the problem of the 'generalized dilution effect' described by Voels et al. We argue that by extension this result may also have implications for the so-called 'helium discrepancy' identified in OB-type stars by Herrero et al.

Key words: line: formation – turbulence – stars: abundances – stars: atmospheres – stars: early-type – supergiants.

1 INTRODUCTION

Surface compositions represent one of the most powerful diagnostics of the evolutionary status of massive OB stars, and should ultimately serve as the instrument of choice for disentangling the relative influences of metallicity, turbulent mixing, convection and rotation in collectively shaping their evolutionary channels. The now-classical O-star analysis involves using plane-parallel, hydrostatic, non-LTE H/He model atmospheres to find a single set of atmospheric parameters $T_{\rm eff}$, $\log_{10}g$ and y that best reproduces observations of selected H I, He I and He II lines (Kudritzki 1976). The He I lines play a crucial role in this respect, as a constraint on y, and yet previous studies have encountered significant line-to-line inconsistencies when standard models are applied to luminous OB stars. For example, Voels et al. (1989) have shown that singlet and triplet lines are systematically discrepant, with the latter being anomalously strong in luminous O stars; they attribute this so-called 'generalized dilution effect' to the extended nature of supergiant atmospheres. The practical significance of these inconsistencies, as Lennon (1994) has highlighted, is that it is difficult to ascribe any degree of confidence to the helium abundances derived for OB supergiants in this way.

In an attempt to sidestep these problems, our previous analyses have concentrated on He I singlet lines, which are intrinsically weaker than the triplets and which, as an ensemble, tend to yield better consistency with the other diagnostics (Smith & Howarth 1994; Smith 1997). Taken in isolation, we find that the weak singlets yield helium number fractions for morphologically normal O stars which are commensurate with the adopted solar (i.e. unevolved) value, whereas the triplets consistently suggest helium enhancements of up to a factor of 2. Nevertheless, even within the singlet system there often remain systematic discrepancies which compromise the analysis: for example, relatively strong lines such as λλ4921 and 4143 typically indicate *higher* helium abundances than weaker lines such as λλ4009 and 5047.

Classically, a systematic discrepancy between weak and strong lines of the same ion can be interpreted as a signature of desaturation owing to intrinsic (e.g. atmospheric or atomic) line broadening. Indeed, evidence for desaturation is frequently encountered in analyses of metallic elements such as CNO and Si in OB-type stars, and is compensated by invoking 'microturbulence' – an ad hoc isotropic atmospheric velocity field with Gaussian velocity distribution and scalelength less than the photon mean free path. For example, recent non-LTE studies of B dwarfs obtain microturbulent velocity amplitudes of up to $10\,\mathrm{km\,s^{-1}}$ (Gies & Lambert 1992), and B supergiants can yield values well in excess of the sound speed (Lennon et al. 1991).

Leaving aside the physical feasibility of the microturbulence concept as applied to the analysis of metallic species, its

concomitant impact on helium line formation[1] appears to have been overlooked. This may be a consequence of the comparatively large thermal velocity of helium and the mitigating influence of pressure broadening on the broad He II and diffuse He I lines used in most analyses. Supergiants are an exception, however, because the implied microturbulent velocities are comparable to the atmospheric thermal velocity [typically $v_{\rm th}({\rm He}) \simeq 10\,{\rm km\,s^{-1}}$], and the electron density (and hence pressure broadening) is low in the line-forming zone (typically $n_{\rm e} \simeq 10^{13}\,{\rm cm^{-3}}$). With this motivation in mind, we investigate in this paper the effect of classical isotropic, Gaussian microturbulence on He I and He II line formation, exploring both its direct influence via line broadening in the radiative transfer, and its indirect influence via changes in the model atmospheric structure and in the statistical equilibrium of the helium atom.

2 NON-LTE MODELS

2.1 Codes and model atoms

Our calculations are based on plane-parallel, hydrostatic, non-LTE atmospheres computed with Hubeny's code TLUSTY, which employs a hybrid complete linearization/accelerated lambda iteration (CL/ALI) method to solve the coupled equations of statistical equilibrium and radiative transfer (Hubeny & Lanz 1995). The model atoms used for the atmospheric structure calculations are similar to those described by Smith & Howarth (1994), based in part on data computed by D. G. Hummer, and comprise 9, 14 and 14 levels for H I, He I and He II, respectively. All frequency points are treated in the ALI scheme except the first few points in each resonant photoionization continuum (i.e. at the bound–free edge) and the central frequency points in selected resonance lines (e.g. Lyα), which are linearized in order to improve convergence. In addition to H and He, CNO ions are included *implicitly* in the calculations for the purpose of number conservation (assuming LTE ionization fractions), but no contribution to either the line or continuum opacity is evaluated for these elements. Convergence is ensured by iteration until the fractional changes in all model quantities (populations, temperature, density, etc.) are smaller than 10^{-3} at every point in the atmosphere.

The atmospheric structures are used as the basis for subsequent statistical equilibrium calculations, also carried out with TLUSTY, and undertaken assuming fixed temperature and pressure distributions. The H/He model atom for this stage is considerably more involved than that employed in the structure calculations (see Smith & Howarth 1994), incorporating all singlet and triplet states of He I with angular momentum quantum number $L \leq 3$ (i.e. S, P, D and F terms) up to principal quantum number $n = 10$ (states with higher L are grouped into one net level for each n). These calculations are carried out assuming Doppler profiles for all line transitions. The validity of that approximation has been demonstrated for O subdwarfs by Rauch & Werner (1988), and should apply with even greater accuracy for O supergiants in which the atmospheric pressures are several orders of magnitude lower (and consequently pressure-broadened line profiles are much narrower).

[1]To avoid confusion, the expression 'line formation' is used here to refer to the complete process of calculating an emergent spectrum *ab initio*; of practical necessity that process implicitly involves several computational steps, the last of which is denoted here by the expression 'line transfer' and is the determination of an emergent spectrum from a *known* atmospheric structure and atomic level populations.

Finally, detailed line transfer calculations are carried out with the fixed populations using the code SURFACE (Giddings 1981; Butler 1984; Butler & Giddings 1985). These calculations utilize full Stark profiles for all line transitions, either by interpolation of pre-tabulated data or by direct computation using Voigt functions. For the diffuse He I lines λλ4026, 4387, 4471 and 4921 we use the tabulated Stark profiles given by Barnard, Cooper & Shamey (1969), Barnard, Cooper & Smith (1974) and Bennet & Griem (1971). These tabulations stop at electron densities of $n_{\rm e} = 3 \times 10^{13}\,{\rm cm^{-3}}$, below which multiple Voigt profiles are assumed, thereby accounting correctly for forbidden and fine-structure components. For the He II lines, the extensive calculations given by Schöning & Butler (1989a,b) are used.

At each stage in the calculations, microturbulent line broadening is readily incorporated in the Doppler and Voigt profiles by modifying the Doppler width $\Delta\lambda_{\rm D}$ to include a non-thermal term thus:

$$\Delta\lambda_{\rm D} = (\lambda/c)\sqrt{(2kT/Am_{\rm H}) + {v_{\rm turb}}^2}, \qquad (1)$$

where c is the speed of light, k is Planck's constant, T is the gas temperature, A is the atomic mass number (of He in this case), $m_{\rm H}$ is the mass of an H atom, and $v_{\rm turb}$ is the microturbulent velocity. The tabulated Stark profiles need special treatment, however, as they were computed assuming pure thermal broadening and therefore require convolution with Gaussian functions of appropriate velocity dispersion. In the model structure calculations, TLUSTY evaluates the contribution of turbulent pressure to the total pressure using the following expression:

$$P_{\rm turb} = \rho {v_{\rm turb}}^2/2, \qquad (2)$$

where ρ is the mass density.

2.2 Equivalent widths

We have explored the influence of microturbulence on the helium lines listed in Table 1 using a $T_{\rm eff} = 32\,{\rm kK}$, $\log_{10} g = 3.0$, $y = 0.09$ model structure, these parameters being typical of the morphologically normal late O supergiants studied by Smith, Howarth & Siebert (1998). Microturbulent velocities of $v_{\rm turb} = 0$, 5, 10 and $15\,{\rm km\,s^{-1}}$ were used in order to examine the sensitivity of equivalent widths, line profiles and level populations to this parameter at velocity amplitudes comparable to those derived from analyses of metallic species in early-type stars (Gies & Lambert 1992). Four sets of calculations were carried out in order to disentangle the relative influence on line strengths of changes in the radiation

Table 1. Helium lines in the blue–visual spectra of O stars.

Ion	λ (Å)	Transition	g_i	g_j	f_{ij}
He I	4009.270	$2p\,^1P^o \rightarrow 7d\,^1D$	3	5	0.0119
	4143.759	$2p\,^1P^o \rightarrow 6d\,^1D$	3	5	0.0209
	4387.928	$2p\,^1P^o \rightarrow 5d\,^1D$	3	5	0.0431
	4921.929	$2p\,^1P^o \rightarrow 4d\,^1D$	3	5	0.1200
	5047.736	$2p\,^1P^o \rightarrow 4s\,^1S$	3	1	0.0084
	4026.189	$2p\,^3P^o \rightarrow 5d\,^3D$	9	15	0.0469
	4471.477	$2p\,^3P^o \rightarrow 4d\,^3D$	9	15	0.1227
	4713.143	$2p\,^3P^o \rightarrow 4s\,^3S$	9	3	0.0106
He II	4199.830	$n = 4 \rightarrow 11$	32	242	0.0082
	4541.590	$n = 4 \rightarrow 9$	32	162	0.0187
	5411.524	$n = 4 \rightarrow 7$	32	98	0.0655
	4685.682	$n = 3 \rightarrow 4$	18	32	0.8421

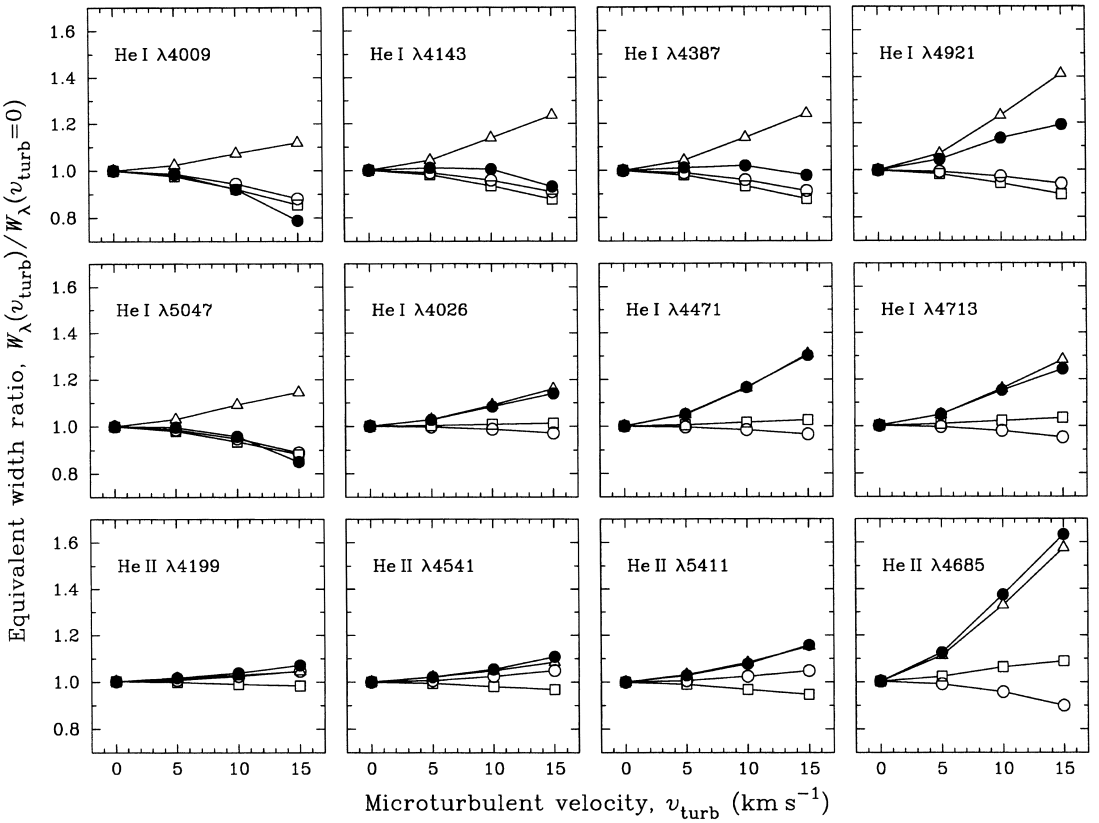

Figure 1. Effect of microturbulence on equivalent widths of selected He I and He II lines. The ratio of equivalent widths $W_\lambda(v_{turb})/W_\lambda(v_{turb}=0)$ is plotted as a function of microturbulent velocity v_{turb}. Results are shown for four sets of calculations: (1) microturbulence in line transfer only (open triangles); (2) microturbulence in statistical equilibrium only (open squares); (3) microturbulence in atmospheric structure only (open circles); and (4) microturbulence self-consistently introduced in *all* calculation steps (filled circles).

transfer, statistical equilibrium and atmospheric structure: the first set introduces microturbulence in the detailed line transfer calculations only, assuming $v_{turb} = 0\,km\,s^{-1}$ in all other steps; the second set introduces microturbulence in the statistical equilibrium calculations only, assuming $v_{turb} = 0\,km\,s^{-1}$ in all other steps; the third set introduces microturbulence in the atmospheric structure calculations only, assuming $v_{turb} = 0\,km\,s^{-1}$ in all other steps; and the fourth set introduces microturbulence consistently throughout. Results from these four sets of calculations are summarized in Fig. 1, which plots the ratio of equivalent widths computed assuming zero and non-zero values of v_{turb} [denoted $W_\lambda(v_{turb}=0)$ and $W_\lambda(v_{turb})$ respectively] as a function of microturbulent velocity. The scaling facilitates comparisons between lines of widely varying strengths, and was applied in each case by dividing through by the equivalent width obtained assuming $v_{turb} = 0\,km\,s^{-1}$.

The direct effect of microturbulence on equivalent widths owing to line broadening in the radiation transfer is to increase the absorbing bandwidth of lines, and thereby increase the equivalent widths of saturated transitions. The magnitude of this effect for the helium lines of interest can be appreciated from the first set of calculations, represented by open triangles in Fig. 1. For the He I lines the increases in equivalent width range between 10 and 40 per cent at $v_{turb} = 15\,km\,s^{-1}$, and are proportionally greater in the triplet transitions. The diffuse triplet line λ4026 is somewhat of an exception, partly because its absorbing bandwidth is intrinsically large owing to the presence of a relatively strong forbidden component at 4025.49 Å (see Fig. 2, later). The strengths of the Fowler series He II lines λλ4199, 4541, and 5411 show a comparatively weak response to microturbulence, with increases of up to 10 per cent, whereas the Pickering line λ4685 exhibits a 60 per cent increase at $v_{turb} = 15\,km\,s^{-1}$.

The indirect effect of microturbulence on equivalent widths owing to changes in level populations is illustrated in the second set of calculations, represented by open squares in Fig. 1. For the He I singlet lines, population changes lead to a modest decrease in equivalent width with increasing microturbulent velocity; this effect is typically between 10 and 15 per cent at $v_{turb} = 15\,km\,s^{-1}$. By contrast, for He I triplet lines, population changes lead to a very small increase in equivalent width with increasing microturbulence (typically a few per cent at $v_{turb} = 15\,km\,s^{-1}$). The Fowler series He II lines marginally decrease in strength with increasing v_{turb}, whereas the Pickering series line λ4685 increases by about 10 per cent at $v_{turb} = 15\,km\,s^{-1}$.

The indirect effect of microturbulence on equivalent widths owing to changes in the atmospheric structure is illustrated in the third set of calculations, represented by open circles in Fig. 1. For the He I singlet lines, structure changes lead to a modest diminution of equivalent width with increasing microturbulent velocity; this effect is typically around 10 per cent at $v_{turb} = 15\,km\,s^{-1}$. The He I triplet lines exhibit a somewhat weaker response to microturbulence-induced structure changes (decreases of a few per cent at $v_{turb} = 15\,km\,s^{-1}$). The Fowler series He II lines marginally increase in strength with increasing v_{turb} (approximately 5 per cent at $v_{turb} = 15\,km\,s^{-1}$), whereas the equivalent width of the

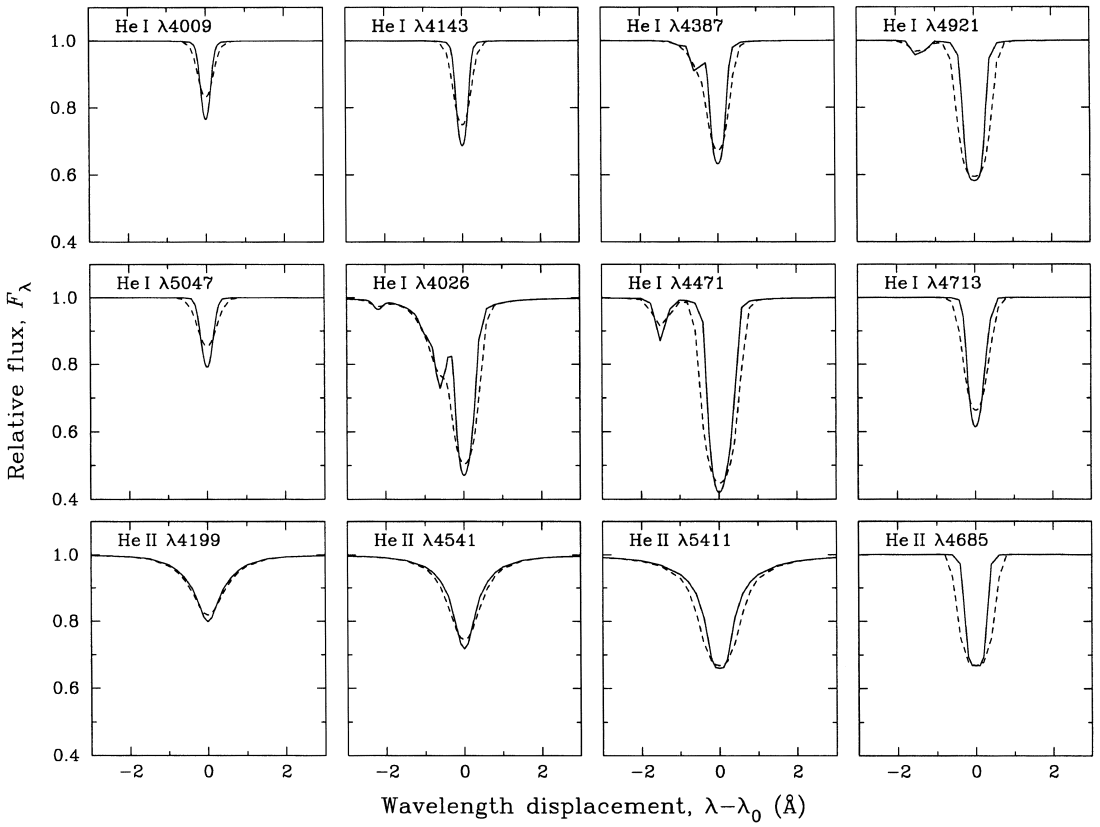

Figure 2. Effect of microturbulence on emergent flux profiles of selected He I and He II lines. Profiles computed assuming $v_{\rm turb} = 0\,{\rm km\,s^{-1}}$ (solid curves) and $v_{\rm turb} = 15\,{\rm km\,s^{-1}}$ (dashed curves) are compared (in order to isolate line transfer effects, populations computed assuming $v_{\rm turb} = 0\,{\rm km\,s^{-1}}$ were used in both cases).

Pickering line λ4685 decreases by about 10 per cent at $v_{\rm turb} = 15\,{\rm km\,s^{-1}}$.

The final set of calculations, combining indirect atmospheric structure and statistical equilibrium effects with direct line transfer effects in a fully self-consistent manner, is represented by filled circles in Fig. 1. These effects roughly cancel in the He I singlets λλ4143 and 4387, whereas at $v_{\rm turb} = 15\,{\rm km\,s^{-1}}$ they cause decreases in excess of 10 per cent in the strengths of λλ4009 and 5047 and an increase of nearly 20 per cent in that of λ4921. Microturbulence effects combine in the three He I triplet transitions considered here to yield increases in strength of 10–30 per cent at $v_{\rm turb} = 15\,{\rm km\,s^{-1}}$. These effects also combine in the He II lines to yield increases at $v_{\rm turb} = 15\,{\rm km\,s^{-1}}$ of 5–20 per cent in the Fowler transitions, and in excess of 60 per cent in the Pickering transition.

2.3 Line profiles

The direct effect of microturbulence on emergent flux profiles can be appreciated by considering Fig. 2, which compares lines computed assuming $v_{\rm turb} = 0$ and $15\,{\rm km\,s^{-1}}$. (Calculations made with $v_{\rm turb} = 5$ and $10\,{\rm km\,s^{-1}}$ yield profiles which are intermediate between those shown in Fig. 2.) In order to isolate line transfer effects, these profiles were calculated using level populations that were obtained assuming $v_{\rm turb} = 0\,{\rm km\,s^{-1}}$. The extent of microturbulent broadening on the linewidths is primarily dependent on the *gradient* of the profiles. More specifically, lines with steep wings, irrespective of the overall linewidth, are most susceptible to broadening; notable examples of such are He I λ4921 and He II λ4685, both of which are broad with steep-sided profiles. Conversely, shallow-winged profiles such as He II λ4199 and (to a lesser extent) He II λ4541 are only marginally perturbed by microturbulent broadening.

Furthermore, a distinction may be drawn between lines with unsaturated and saturated cores, the relative intensities of which respond differently to increasing $v_{\rm turb}$: for example, at $v_{\rm turb} = 15\,{\rm km\,s^{-1}}$ the increased absorbing bandwidth in the weak He I singlets occurs at the expense of core absorption, whereas in the saturated triplets the core depths are almost invariant. To avoid possible confusion, we stress that these remarks on core depths apply only to the *intrinsic* profiles. For many luminous, early-type stars the *observed* line profiles are dominated by rotation (Conti & Ebbets 1977; Howarth et al. 1997), and in this situation the only way to accommodate an increase in equivalent width is by an increase in line depth. Thus the net effect of convolving the profile of a line such as He I λ4713 with a rotational broadening function having $v \sin i \gg v_{\rm turb}$ is an increase in line depth (even though the intrinsic profile is shallower).

2.4 Level populations

Microturbulence has an influence on the statistical equilibrium of He I/He II via changes in the optical depths (and thence the radiative rates) of saturated transitions. More specifically, large values of $v_{\rm turb}$ decrease the optical depths in opaque transitions by providing a greater frequency bandwidth for escaping photons. By way of illustration of this point, we have determined the mass depths at

Table 2. Mass depths at which the monochromatic optical depth of line centre radiation equals 2/3.

Line		$m(\tau_\nu=2/3)$ (gm cm^{-2})	
		$v_{\rm turb}=0$ km s^{-1}	$v_{\rm turb}=15$ km s^{-1}
He I	λ4009	6.58×10^{-1}	8.53×10^{-1}
	λ4143	4.72×10^{-1}	6.28×10^{-1}
	λ4387	3.36×10^{-1}	4.43×10^{-1}
	λ4921	1.93×10^{-1}	2.44×10^{-1}
	λ5047	6.83×10^{-1}	8.73×10^{-1}
	λ4026	1.68×10^{-1}	2.16×10^{-1}
	λ4471	1.02×10^{-1}	1.28×10^{-1}
	λ4713	3.29×10^{-1}	4.36×10^{-1}
He II	λ4199	5.37×10^{-1}	6.23×10^{-1}
	λ4541	2.58×10^{-1}	3.55×10^{-1}
	λ5411	7.80×10^{-2}	1.16×10^{-1}
	λ4685	1.43×10^{-2}	1.79×10^{-2}

which the line centre monochromatic optical depths are 2/3 for the transitions listed in Table 1. These quantities, $m(\tau_\nu=2/3)$, indicate the depths at which photons have a 50 per cent probability of free escape, which we can identify with the line-forming zone of the atmosphere. The calculations, which are presented in Table 2, show that $m(\tau_\nu=2/3)$ differs by about 30 per cent between the two extreme values of microturbulent velocity considered ($v_{\rm turb}=0$ and 15 km s^{-1}).

The effect of microturbulence on the populations of selected He I and He II states is illustrated in Fig. 3, which plots the ratio of populations computed assuming zero and non-zero values of $v_{\rm turb}$ [denoted $n(v_{\rm turb}=0)$ and $n(v_{\rm turb})$ respectively] as a function of mass depth. In the interests of brevity, results are shown only for states that are involved in the transitions listed in Table 1, and thereby *directly* influence their strength. The line formation zone can be gauged from the vertical tick marks which indicate the $v_{\rm turb}=0$ km s^{-1} values of $m(\tau_\nu=2/3)$ from Table 2, these differing imperceptibly from the $v_{\rm turb}=15$ km s^{-1} values on the logarithmic scale used.

Fig. 3 clearly shows that the influence of microturbulence on level populations is sensitively dependent on the magnitude of $v_{\rm turb}$: small changes are evident at $v_{\rm turb}=5$ km s^{-1}(typically less than 1 per cent), but they are disproportionally larger at $v_{\rm turb}=10$ and 15 km s^{-1} (~5 per cent or more). Within the He I singlet system, the most conspicuous effect of microturbulence is a gross depopulation of the 2p ^{1}P state (up to ~15 per cent at $\log_{10} m\simeq-1.0$). The $n=4$ singlet states exhibit a more complex response to microturbulence, with a weak depopulation 'dip' occurring at $\log_{10} m\simeq-1.0$ and a stronger overpopulation 'peak' at $\log_{10} m\simeq-1.6$; states with $n>4$ exhibit only the overpopulation peak. The triplet system responds more uniformly to microturbulence, with all states showing some degree of overpopulation: the low-energy state 2p ^{3}P has a broad overpopulation peak at mass depths between 0 and −2 dex, whereas the $n\geq4$ states exhibit relatively sharp overpopulation peaks centred at $\log_{10} m\simeq-1.7$. Microturbulence also depopulates the excited ($n\geq3$) states of He II in the line-forming zone at mass depths between 0 and −2 dex, by up to 14 per cent for an assumed $v_{\rm turb}=15$ km s^{-1}. The depopulation dip seen in the $n=3$ state is relatively sharp and high in the atmosphere when compared with that observed in the $n=4$ state. The depopulation pattern is repeated in more highly excited states, but decreases in magnitude with increasing n.

The influence of changes in populations on line strengths can be crudely understood using the following expression for the line absorption coefficient (Mihalas 1978, equation 10-2):

$$\chi_{\rm l}=(\pi e^2/mc)f_{ij}[n_i-(g_i/g_j)n_j], \tag{3}$$

where f_{ij} is the (absorption) oscillator strength for transitions from lower state i to upper state j; n_i and n_j are the populations, and g_i and g_j the statistical weights, of the lower and upper states respectively; and all other symbols take their conventional meanings. The line opacity contributes to the optical depth scale, $d\tau_\nu\equiv-(\kappa_{\rm c}+\sigma+\chi_{\rm l}\phi_\nu)dz$, and hence the equivalent width via the emergent flux integral:

$$F_\nu=2\int_0^\infty S_\nu(\tau_\nu)E_2(\tau_\nu)\,d\tau_\nu, \tag{4}$$

where $\kappa_{\rm c}$ and σ are the continuum opacity and scattering coefficient respectively, ϕ_ν is the absorption-line profile, S_ν is the source function, and E_2 is the second exponential integral. Under the assumption of LTE, the source function is equal to the Planck function at the local temperature ($S_\nu\equiv B_\nu$). If the photosphere is characterized by a negative temperature gradient (as is the case for mass depths $\log_{10} m>-1$), increases in τ_ν drive line formation to higher, cooler strata and the equivalent widths of absorption lines *increase*. To some extent that situation is complicated in the more general (non-LTE) case of interest here by the fact that the source function is not tied to the temperature structure of the atmosphere – it is determined by a self-consistent solution of the coupled transfer and statistical equilibrium equations.

All of the singlet lines of spectroscopic interest listed in Table 1 are transitions involving 2p ^{1}P$^{\rm o}$ as the lower state, and most connect to upper states of the form nd ^{1}D. In the line-forming zone, microturbulence depopulates the lower state 2p ^{1}P$^{\rm o}$ and (to a much lesser extent) the upper states such as nd ^{1}D. The lower state dominates equation (3) because $n_i>n_j$ and (in most cases) $g_i/g_j<1$. Thus microturbulence decreases the line opacity for these transitions, with a corresponding decrease in the calculated equivalent widths, as seen in Fig. 1.

The triplet lines listed in Table 1 are transitions involving 2p ^{3}P$^{\rm o}$ as the lower state, which is selectively overpopulated by microturbulence in the line-forming zone indicated in Fig. 3. Again there are corresponding population changes in the upper states of these transitions (e.g. nd ^{3}D), but they are rather small in the line-forming zone. The net effects of these changes, allowing for the statistical weight factors mentioned above, are small increases in the line opacity. However, because the triplet lines are heavily saturated, these population changes are not reflected in substantially increased equivalent widths.

The Fowler series He II lines are transitions involving $n=4$ as the lower state, which is heavily depopulated by microturbulence in the line-forming zone. The upper states of these transitions are also depopulated by microturbulence, but the $n=4$ state dominates equation (3) so the line opacity decreases with increasing $v_{\rm turb}$. There are corresponding decreases in the calculated equivalent widths seen in Fig. 1, although these are comparatively small owing to saturation effects.

The Pickering series line λ4685 is a more complex case: although microturbulence induces a net depopulation of the $n=3$ and 4 states, so that the line opacity decreases, there is a paradoxical *increase* in the calculated equivalent widths. As Fig. 4 illustrates, that population-associated increase in equivalent width occurs when a decrease in the residual flux of the line core is countered by an increase in the residual flux in the line wing. (Note that, as in

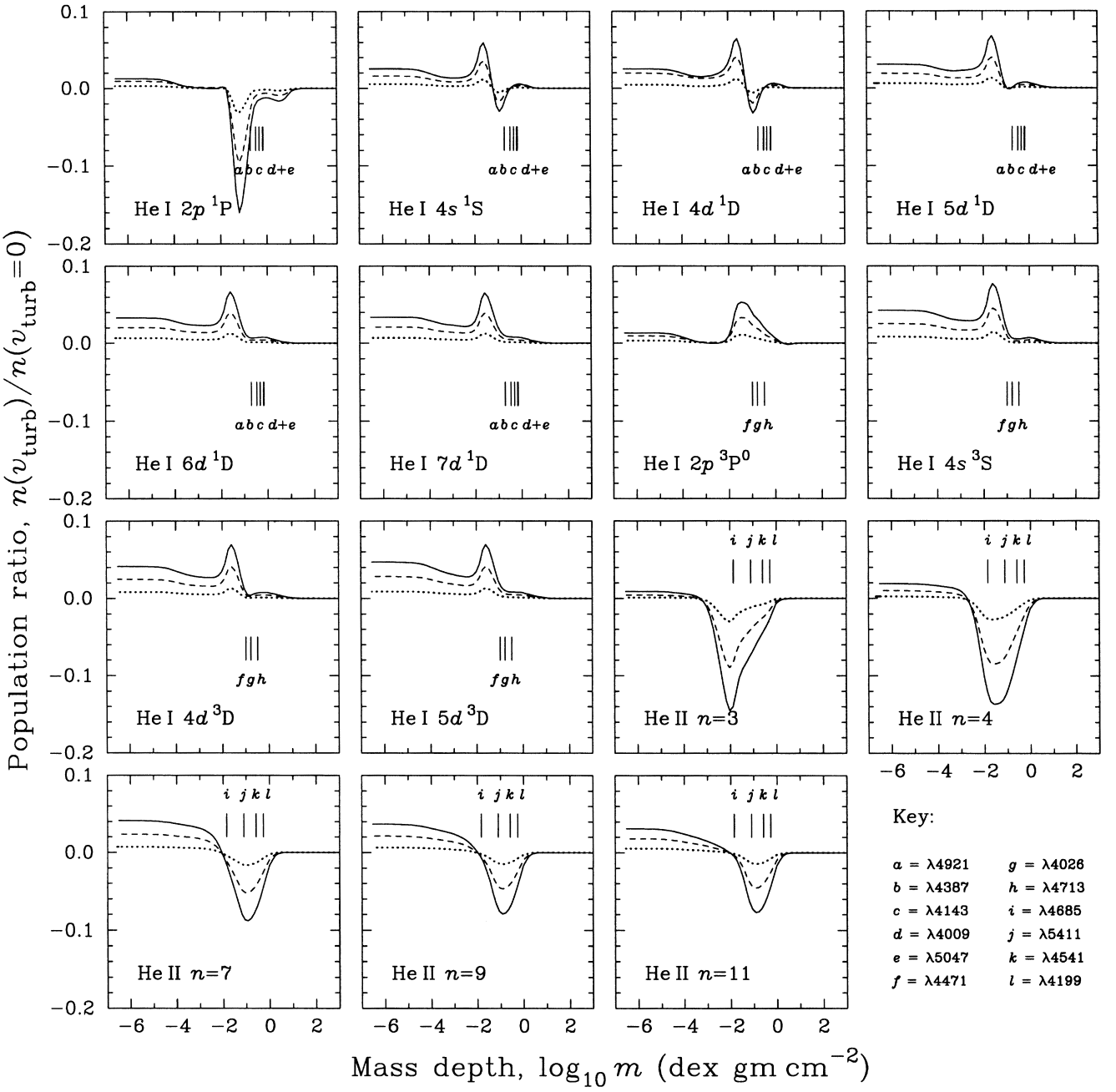

Figure 3. Effect of microturbulence on level populations for selected He I and He II states. The ratios of populations computed assuming $v_{\rm turb} = 0\,{\rm km\,s^{-1}}$ and $v_{\rm turb} = 5\,{\rm km\,s^{-1}}$ (dotted curves), $v_{\rm turb} = 10\,{\rm km\,s^{-1}}$ (dashed curves) or $v_{\rm turb} = 15\,{\rm km\,s^{-1}}$ (solid curves) are plotted as a function of logarithmic mass depth. The vertical tick marks, which are labelled alphabetically, mark the depths at which $\tau_\nu = 2/3$ for line centre radiation in the 12 transitions listed in the key (see also Table 2); this gives an indication of the line-forming zone of the atmosphere.

Section 2.2, we have assumed zero microturbulence in the line transfer stage of the calculations illustrated in Fig. 4, so as to isolate the effect of population changes on the emergent flux.) The inverse relationship between the line opacity and emergent flux in the wings of λ4685 arises from a 'dip' in its monochromatic source function at line-forming optical depths ($\tau_\nu < 1$), as can be appreciated from Fig. 5.

2.5 Atmospheric structures

Microturbulence has a direct influence on model atmosphere structures via two routes: (1) the thermodynamic equilibrium through heating/cooling in microturbulence-broadened radiative transitions; and (2) the hydrostatic equilibrium through the turbulent pressure contribution to the total pressure stratification. The magnitude of these effects for our chosen model can be appreciated in Fig. 6, which plots temperature and electron pressure distributions as a function of mass depth for two assumed values of the microturbulent velocity ($v_{\rm turb} = 0$ and $15\,{\rm km\,s^{-1}}$). The temperature stratification is only marginally affected by microturbulence, consistent with expectation for our pure H/He-blanketed models. The $v_{\rm turb} = 15\,{\rm km\,s^{-1}}$ model is associated with a modest increase in radiative heating (2–3 per cent) in the temperature reversal zone of

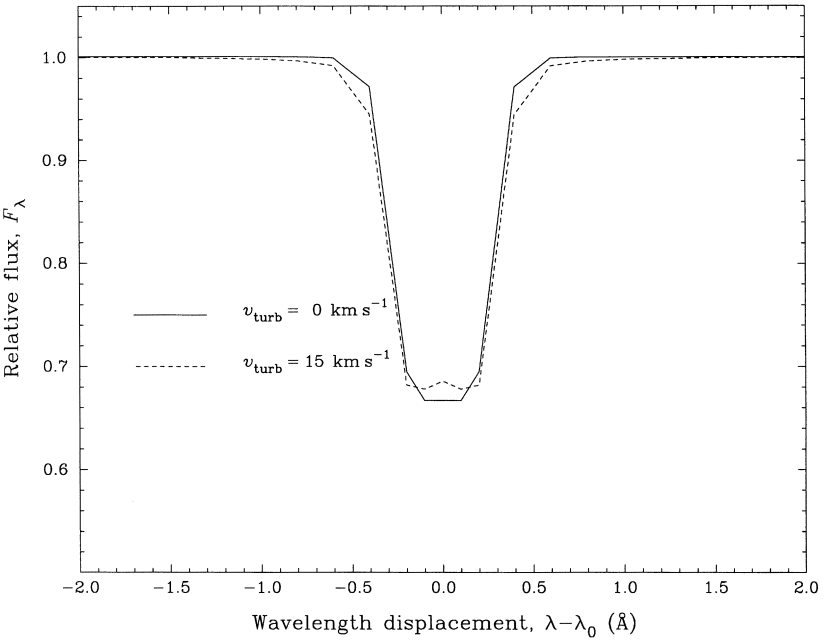

Figure 4. Effect of microturbulence-related population changes on emergent flux profiles of He II λ4685. Line profiles computed using two sets of populations are compared: the first set comprises populations in which $v_{\rm turb} = 0\,{\rm km\,s^{-1}}$ has been assumed (solid curve); the second set comprises populations in which $v_{\rm turb} = 15\,{\rm km\,s^{-1}}$ has been assumed (dashed curve). In both cases, $v_{\rm turb} = 0\,{\rm km\,s^{-1}}$ has been assumed in the line transfer calculation itself.

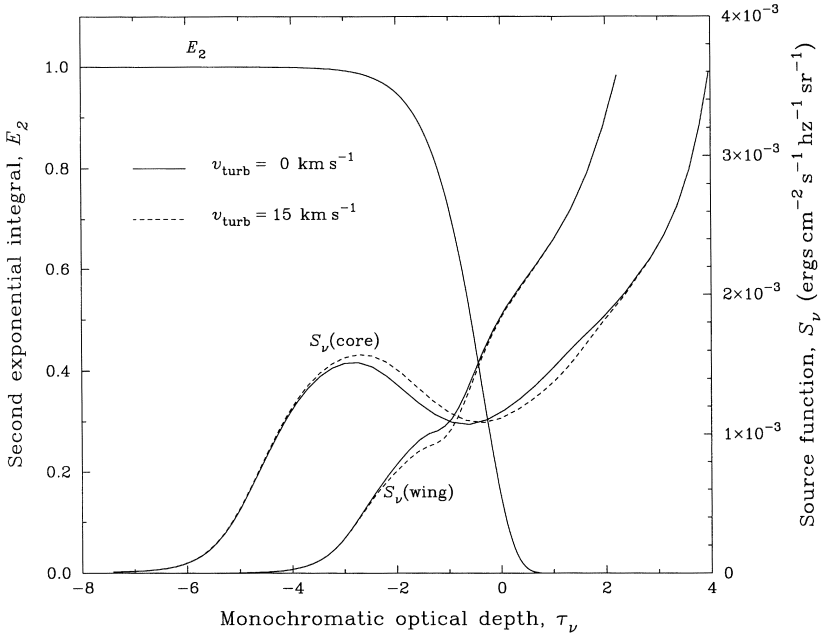

Figure 5. Effect of microturbulence on the source function of He II λ4685 at line centre (4685.682 Å) and in the near-centre wing (4686.082 Å). Total source functions computed assuming $v_{\rm turb} = 0\,{\rm km\,s^{-1}}$ (solid curves) and $v_{\rm turb} = 15\,{\rm km\,s^{-1}}$ (dashed curves) are compared with the second exponential integral function E_2 (right- and left-hand scales respectively).

the atmosphere ($\log_{10} m \simeq -1.5$). Microturbulence will have a considerably greater influence on the thermodynamic equilibrium of fully metal line blanketed models (specifically via increased backwarming), although the consideration of such models is beyond the scope of this paper.

The electron pressure stratification is modified significantly by microturbulence at depths less than $\log_{10} m \simeq 0.0$; the $v_{\rm turb} = 15\,{\rm km\,s^{-1}}$ model is characterized by electron pressures 0.03 dex (~7 per cent) *lower* than the $v_{\rm turb} = 0\,{\rm km\,s^{-1}}$ model at a given mass depth. This effect arises because turbulent pressure partially offsets the 'true' (i.e. particle) gas pressure required hydrostatically to support a fixed column of material against gravity. The photospheric electron pressure in a $v_{\rm turb} = 15\,{\rm km\,s^{-1}}$ model is crudely equivalent to that in a $v_{\rm turb} = 0\,{\rm km\,s^{-1}}$ model with

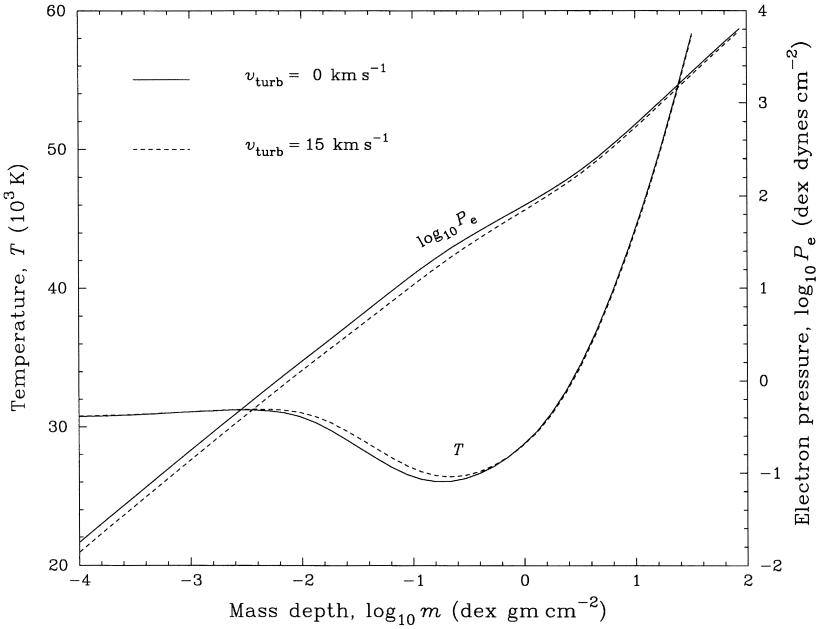

Figure 6. Effect of microturbulence on the temperature distribution (left-hand scale) and electron pressure distribution (right-hand scale) in a solar-composition, H/He-blanketed, $T_{\rm eff} = 32$ kK, $\log_{10} g = 3.0$ model atmosphere. Models computed assuming $v_{\rm turb} = 0\,{\rm km\,s^{-1}}$ (solid curves) and $v_{\rm turb} = 15\,{\rm km\,s^{-1}}$ (dashed curves) are plotted as a function of mass depth.

$\log_{10} g$ lower by $\sim$0.03. This property accounts for the subtle pattern of *structure-associated* effects on equivalent widths described in Section 2.2, where He I lines decrease and (most) He II lines increase in strength with increasing $v_{\rm turb}$.

3 AN ANALYSIS OF HD 152003

The microturbulence effects described in the foregoing section offer an opportunity to reconcile discrepant He I lines in the analysis of luminous OB-type stars by virtue of their differential impact on weak singlets and strong triplets. In order to explore the influence of microturbulence on the diagnostic properties of He I lines, we have extended the three-dimensional model spectrum grid described by Smith & Howarth (1994) to incorporate microturbulent velocity as a fourth parameter. This extension was carried out in a fully self-consistent manner by introducing microturbulence in the model structure, statistical equilibrium and line transfer stages of the calculation. The new grid was computed assuming microturbulent velocities of $v_{\rm turb} = 0$, 5, 10 and 15 km s^{-1}.

By way of illustration, we have applied our extended grid to an analysis of the O9.7 Iab star HD 152003. The observational material for this study comprises high-resolution ($R \simeq 2 \times 10^4$), high signal-to-noise ratio (> 200) spectra acquired using the University College London Echelle Spectrograph at the Anglo-Australian Telescope during 1992 June (see Smith & Howarth 1994 for details). The analytical procedure involves finding a simultaneous and consistent fit to selected He II, H I and He I lines, which apply constraints on the stellar $T_{\rm eff}$, $\log_{10} g$ and y respectively. For this study we fit to the equivalent widths of the helium lines, rather than the line profiles, thereby sidestepping the determination of an appropriate value for $v \sin i$. (Profile fits are retained, perforce, for the H I lines, but these are only weakly sensitive to the assumed $v \sin i$.)

In carrying out the analysis we have used *all* of the helium lines listed in Table 1, except He II λ4685, which is strongly contaminated by wind emission in luminous OB stars (e.g. Gabler et al. 1989). The principal tools of the analysis are $T_{\rm eff}$–$\log_{10} g$ diagrams at fixed values of y and $v_{\rm turb}$ – two-dimensional slices in the four-dimensional parameter space of the model grid – upon which are superimposed curves which correspond to fits to individual lines. Examples of such diagrams, in this case computed assuming a solar helium number fraction ($y = 0.09$) and four values of microturbulent velocity ($v_{\rm turb} = 0$, 5, 10 and 15 km s^{-1}), are presented in Fig. 7. Fits to the neutral and ionized helium lines are represented by loci of constant equivalent width *exactly* matching those determined from the observations, whereas fits to the wings of the hydrogen lines are represented by curves of minimum χ^2.

As Fig. 7 illustrates, there is a remarkable improvement in consistency between the He I diagnostics with increasing $v_{\rm turb}$ (at fixed y). At low values of $v_{\rm turb}$ the singlet lines of He I yield acceptable internal agreement, whereas the triplets are both internally discordant and displaced to anomalously high gravities. It is not possible to obtain any fit to the observed equivalent width of the triplet λ4713 at microturbulent velocities below 10 km s^{-1}, within the parameter domain illustrated (i.e. $T_{\rm eff} = 27$–37 kK, $\log_{10} g = 2.7$–3.7). However, it should be noted that λ4713 is, in fact, a poor temperature and gravity discriminant, being only very weakly sensitive to either parameter (cf. Simon 1991); consequently, observational and analytical errors tend to induce relatively large displacements of its diagnostic tracks in the $T_{\rm eff}$–$\log_{10} g$ plane. The anomalous behaviour of the triplets at low values of microturbulent velocity is reflective of the fact that the model predictions for these lines (in particular for λ4471) are too weak as compared with the observations – an apparently universal feature of the O supergiants that we have analysed to date.

The weaker triplets λλ4026 and 4713 are brought into good agreement with the singlets at $v_{\rm turb} = 10\,{\rm km\,s^{-1}}$, whereas the strong triplet λ4471 only becomes acceptably consistent at $v_{\rm turb} = 15\,{\rm km\,s^{-1}}$. Experience suggests that further fine tuning of the helium number fraction and microturbulent velocity can

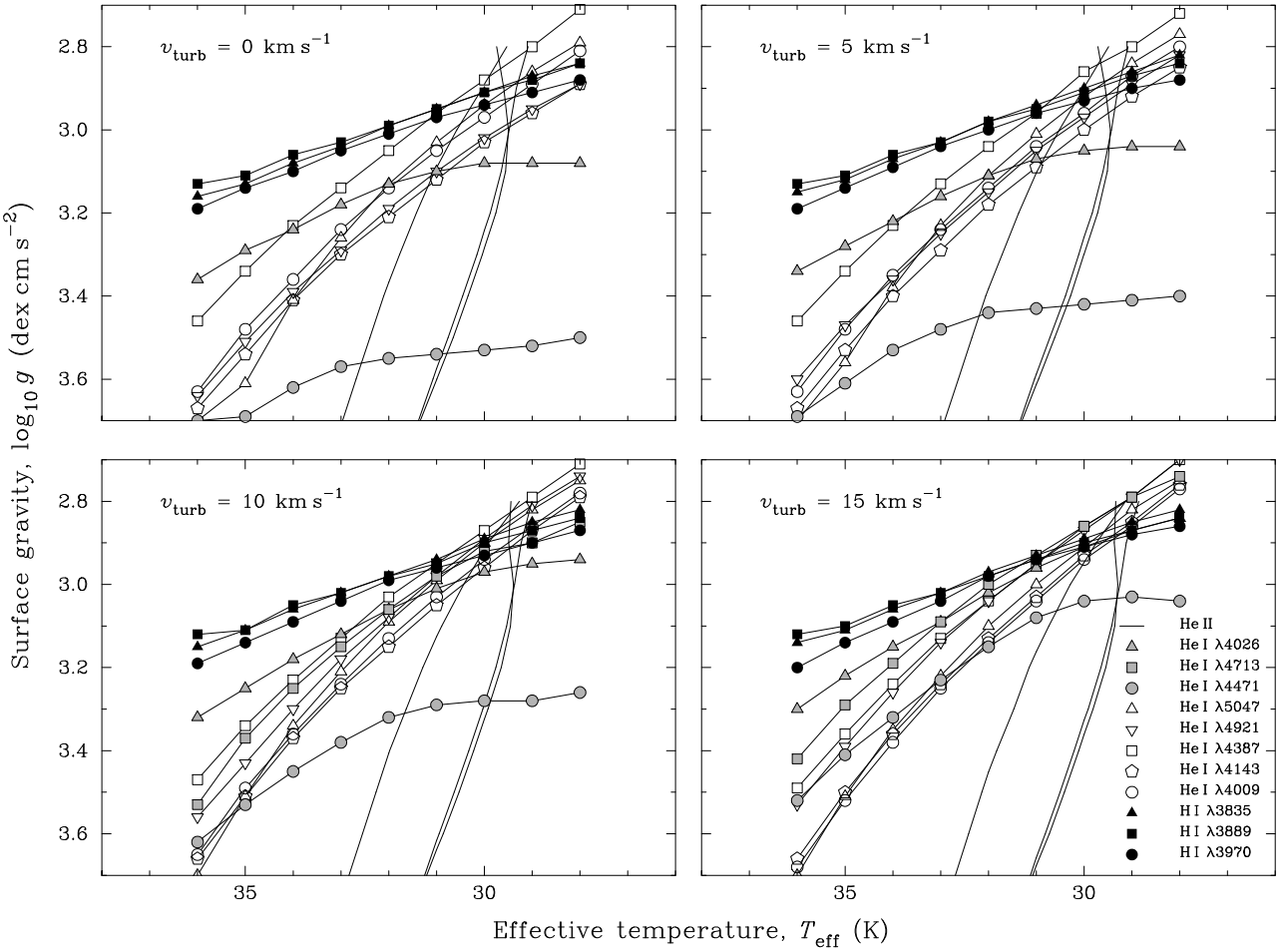

Figure 7. Effective temperature–surface gravity diagrams for HD 152003 derived for helium number fraction $y = 0.09$, and assuming four values of the microturbulent velocity $v_{\rm turb}$ as indicated. The curves represent loci of constant equivalent width for the helium lines, and of minimum χ^2 for the hydrogen lines. Note the improved consistency between the He I singlets and triplets (especially λ4471) with increasing $v_{\rm turb}$, and the absence of a fit to the observed equivalent width of λ4713 at both $v_{\rm turb} = 0$ and 5 km s^{-1}.

Table 3. Best-fitting model parameters for HD 152003.

$v_{\rm turb}$ (km s^{-1})	$T_{\rm eff}$ (kK)	$\log_{10} g$ (dex cm s^{-2})	rms p (kK)
0	30.8 ± 0.6	3.10 ± 0.13	1.466
5	30.5 ± 0.5	3.04 ± 0.12	1.248
10	30.3 ± 0.4	2.98 ± 0.09	0.952
15	29.7 ± 0.2	2.90 ± 0.04	0.468

improve the overall consistency of *all* the diagnostics at the expense of assuming a slightly subsolar value of y and super-thermal value of $v_{\rm turb}$. Such behaviour highlights the inverse relationship between the assumed value of $v_{\rm turb}$ and the derived value of y. However, it is interesting to note that manipulation of the assumed values of $v_{\rm turb}$ and y impacts little on the derived values of $T_{\rm eff}$ and $\log_{10} g$, as inferred from the intersection of the He II and H I diagnostics.

Table 3 lists the best-fitting model parameters $T_{\rm eff}$ and $\log_{10} g$ for each value of $v_{\rm turb}$. The fit parameters were optimized by a numerical procedure which finds that point in the $T_{\rm eff}$–$\log_{10} g$ plane for which the root-mean-square distance to the diagnostic tracks is a minimum. Implicit in this procedure is a normalization of the axes in order to make them dimensionally commensurate; in practice, we normalize the $\log_{10} g$ axis by the factor $f = 10\,{\rm kK/dex(cm\,s^{-2})}$, which is approximately the sensitivity ratio $\delta T_{\rm eff}/\delta \log_{10} g$. Thus, for any $T_{\rm eff}$–$\log_{10} g$ diagram such as is illustrated in Fig. 7, we find the normalized parameters $t_0 = T_{\rm eff}$ and $g_0 = f \log_{10} g$ that minimize the quantity rms p (in units of kK) defined by

$$\mathrm{rms}\,p = \frac{1}{\sqrt{N}} \left[\sum_{i=1}^{N} (t_i - t_0)^2 + (g_i - g_0)^2 \right]^{1/2}, \qquad (5)$$

where (t_i, g_i) is the point of closest approach of diagnostic track i (of which there are N in total) to the point (t_0, g_0). The quantity rms p is essentially the dispersion of the diagnostic tracks about the best-fitting point. Uncertainties on the best-fitting $T_{\rm eff}$ and $\log_{10} g$ are estimated by computing the resolved components of rms p, which we have verified by Monte Carlo simulations.

In computing the best-fitting model parameters listed in Table 3, use has been made of *all* the He I lines including λ4471 which, as can be appreciated from Fig. 7, is a conspicuous outlier for all values of $v_{\rm turb}$ below 15 km s^{-1}. The influence of the discrepant λ4471 is to bias the solution to anomalously high gravities, although

Table 4. Observed and best-fitting model ($v_{\rm turb} = 15\,{\rm km\,s^{-1}}$) equivalent widths compared.

Line	W_λ (mÅ)		Line	W_λ (mÅ)	
	obs	mod		obs	mod
He I λ4009	128	121	He I λ4471	699	658
He I λ4143	185	182	He I λ4713	248	276
He I λ4387	250	314	He II λ4199	152	162
He I λ4921	389	452	He II λ4541	181	211
He I λ5047	113	121	He II λ5411	318	308
He I λ4026	594	597			

the derived effective temperatures (which are primarily fixed by the He II lines) are largely unaffected. The values of rms p – which are a measure of the 'goodness of fit' – decrease monotonically with increasing $v_{\rm turb}$, lending quantitative support to our assertion that the introduction of microturbulence significantly improves the consistency of the He I diagnostics.

The best-fitting model obtained within the grid for HD 152003, assuming a helium number fraction $y = 0.09$, is $T_{\rm eff} = 29.7\,{\rm kK}$, $\log_{10} g = 2.90$ at $v_{\rm turb} = 15\,{\rm km\,s^{-1}}$. In Table 4 we compare the observed equivalent widths of helium lines with those predicted by this best-fitting model. We conservatively estimate that the observed values are uncertain by 10 per cent, primarily owing to unaccounted contaminating blends; on that assumption the reduced chi-squared for the best-fitting model is $\chi^2_\nu = 1.86$ for $\nu \equiv N - 3 = 8$ degrees of freedom. Note that the best-fitting model systematically overestimates the strengths of the weaker He I diagnostics, suggesting that a slightly lower value of y (coupled with a still higher value for $v_{\rm turb}$) could be appropriate, as suggested above.

A visual impression of the accuracy of the best-fitting model can be gained from Fig. 8, which compares predicted profiles of the diagnostic lines with observations. Note that, in order to simulate macroscopic line broadening, the model profiles have been convolved with a Gaussian function rather than the conventional rotation function. We find that, for most of the O supergiants in the Smith et al. (1998) sample, Gaussian functions yield superior

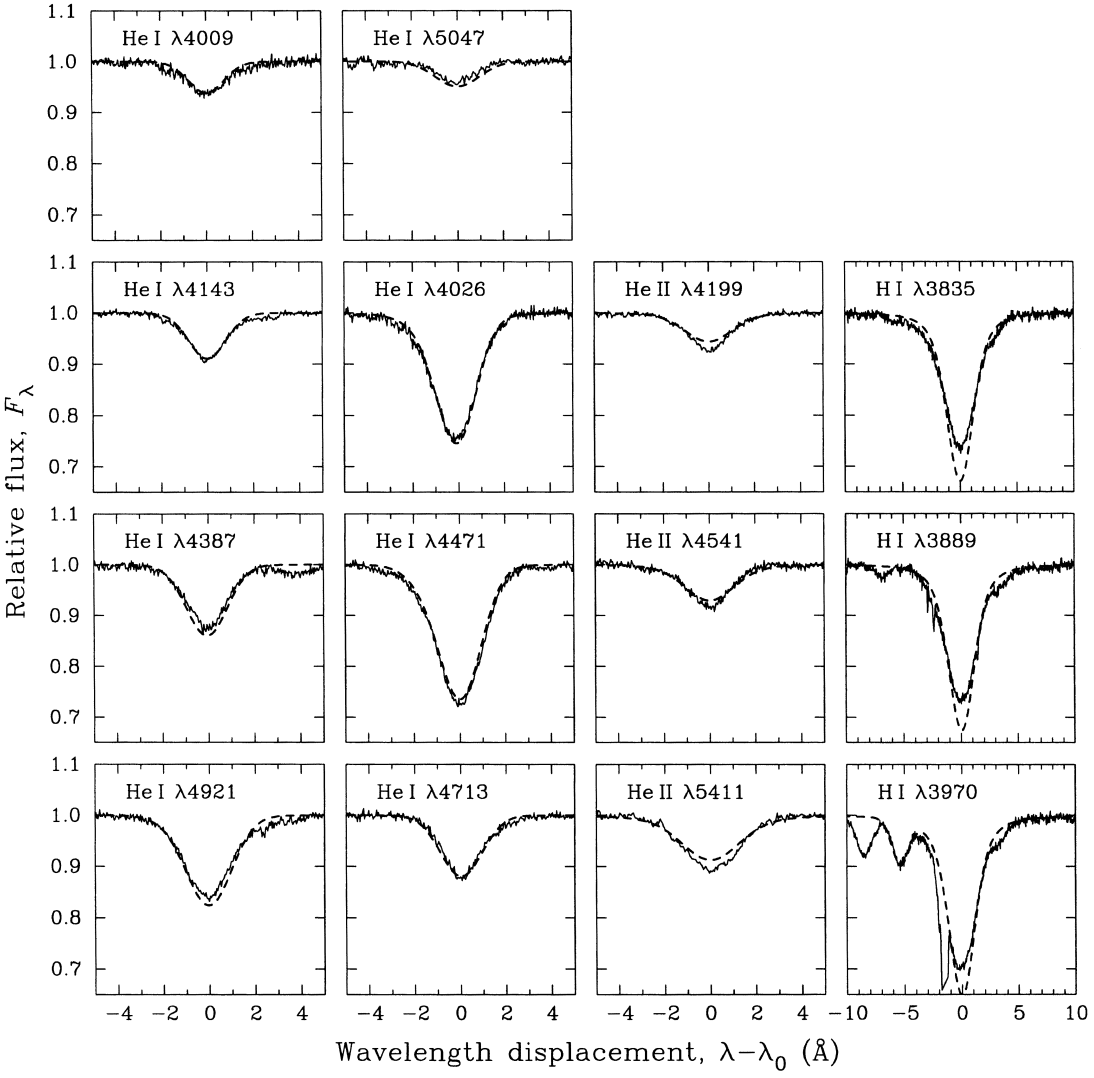

Figure 8. Predicted line profiles (dashed curves) from the best-fitting solar-composition model ($T_{\rm eff} = 29.7\,{\rm kK}$, $\log_{10} g = 2.90$, $v_{\rm turb} = 15\,{\rm km\,s^{-1}}$) compared with observations of HD 152003 (solid curves). The predicted profiles have been convolved to allow for stellar macroscopic broadening. Note that the cores of the predicted hydrogen Balmer profiles are systematically deeper than the observations; only the wings were used for the fits. The strong feature blueward of λ3970 (Hε) is the interstellar Ca II H line.

fits over classical rotation functions – a property which is presumably attributable to the combination of line broadening processes (rotational + outflow + turbulence?) characteristic of the atmospheres of such luminous stars. For HD 152003 we obtain a mean Gaussian velocity dispersion of $79 \pm 10\,\mathrm{km\,s^{-1}}$ (s.e.) based on least-squares fits of convolved model profiles to the eight 'cleanest' He I lines; this is comparable to the mean $v \sin i$ of $93 \pm 10\,\mathrm{km\,s^{-1}}$ (s.e.) derived by fitting rotationally broadened profiles to the same lines.

Fig. 8 shows that the strong He I triplets are well matched by the model, perhaps at the expense of the fit to some of the singlets (e.g. λλ4387, 4921, 5047) which are weaker than predicted. The cores of the He II lines are stronger, and their wings weaker than predicted by the model, but, as Table 4 supports, they are on average well matched in total strength. Of particular concern are the Balmer lines, which are fitted well in the wings (as expected given that this was a criterion of constraint in deriving the best-fitting parameters), but have conspicuously shallower cores than predicted by the model – possibly due to 'in-filling' by emission from the stellar wind (cf. Smith & Howarth 1994).

4 DISCUSSION

4.1 The helium discrepancy

The 'helium discrepancy' is a pattern of surface helium enrichments in OB-type stars discussed by Herrero et al. (1992). They found y values in excess of 0.12 in nearly all supergiants and in some rapidly rotating dwarfs in a sample of about 40 Galactic OB stars. However, their analysis was based primarily on the strong singlet λ4921, with λ4387 as a 'fall-back' in problematic cases. As this paper demonstrates, λ4921 is exceptionally sensitive to microturbulence, because of the combination of its steep-sided profile and degree of saturation. It is therefore tempting to speculate that the helium discrepancy may be attributable – at least in OB supergiants – to the use of λ4921 as a determinant of y. There is some support for that assertion from an analysis of 11 late O Galactic supergiants, which was carried out using a grid of non-LTE models incorporating microturbulence in the line transfer calculations only (Smith et al. 1998). In that study, consistency arguments applied to the He I diagnostics (singlets only) coupled with a non-LTE curve-of-growth analysis of CNO lines suggested that microturbulent velocities of $\sim 15\,\mathrm{km\,s^{-1}}$ are appropriate for these stars; on that assumption *nearly all* morphologically normal O supergiants can be characterized by solar helium number fractions. The same mechanism should also be effective in the slightly cooler B supergiants, which are characterized by stronger (i.e. more saturated) He I lines than the late O counterparts discussed here (see e.g. Lennon, Dufton & Fitzsimmons 1992, 1993), as discussed in an independent study by McErlean, Lennon & Dufton (1998). Although a fully self-consistent treatment of microturbulence in our analyses will probably require modifications of the derived parameters in detail – including the value of v_{turb} – preliminary results suggest that our conclusion that, in general, O supergiants are not substantially helium-enriched will hold. However, it should be noted that microturbulence appears not to be capable of explaining the spectra of the ON-type stars, for which we still find helium enrichments coupled with modifications of the CN abundances indicative of the presence of nucleosynthetically processed material.

Our calculations suggest that microturbulent velocities of $5\,\mathrm{km\,s^{-1}}$ or less have a small (possibly negligible) influence on the He I spectra of OB supergiants. Extrapolating that conclusion to higher surface gravities, which are associated with correspondingly broader photospheric lines, suggests that microturbulence is unlikely to prove an effective mechanism in explaining away helium enrichments in most OB dwarfs. On the other hand, for stars at an appreciable fraction of their break-up rotational velocity, there exists an equator-to-pole variation in temperature and effective surface gravity. In such objects, the He I spectrum is dominated by emergent radiation from the relatively cool, low-gravity equatorial belt, whereas the He II spectrum is formed in the hot, high-gravity polar caps. Thus the equatorial zone in rapid rotators may be susceptible to the influence of microturbulence, perhaps to the same extent as giants of comparable effective surface gravity.

4.2 The generalized dilution effect

The generalized dilution effect was first identified observationally by Voels et al. (1989), in a study of O9.5 stars. They found the predicted strengths of certain singlet and triplet He I lines to be too weak, by amounts increasing with both f-value and luminosity, and attributed this to differential overpopulation of the $n = 2$ levels of He I by geometrical dilution in an extended atmosphere, with the states $2s\,^3S$, $2s\,^1S$, $2p\,^3P^o$ and $2p\,^1P^o$ affected in decreasing order. They argued that dilution-induced overpopulation is most important for the strong $n = 2 \rightarrow 3$ transitions λλ5876 and 6678, and to a lesser extent for the $n = 2 \rightarrow 4$ transition λ4471, all of which form higher in the atmosphere than weaker lines such as λ4387.

Dilution effects in λ4471 were subsequently confirmed by Herrero et al. (1992), who found that line to be anomalously strong – as compared with fits to λλ4387 and 4921 – in all the O supergiants that they analysed, about half the giants, and none of the dwarfs. Interestingly, they reported the converse problem in two stars of spectral type O5, wherein λ4471 appears *weaker* than predictions based on fits to λλ4387 and 4921 might suggest. Herrero (1993) has since demonstrated that, for such stars, line blocking in the He I resonance transition $1s\,^1S \rightarrow 2p\,^1P^o$ (584 Å) decreases the atmospheric depth at which the He I singlets are formed, increasing their core residual intensities, and thereby reconciling them with the triplets at somewhat higher temperatures and lower gravities than previously. However, that mechanism is not so effective in O stars of later spectral type where the generalized dilution effect becomes conspicuous. More recently, Herrero et al. (1995) have applied spherical, hydrodynamic ('unified') models in an analysis of the O9.7 Iab star HDE 226868 (the optical counterpart of Cygnus X-1), and showed that the presence of a strong wind is insufficient to resolve the dilution effect observed in λ4471.

Our analysis of a typical late O supergiant suggests that turbulent photospheric velocity fields are in principle capable of largely (if not completely) resolving the generalized dilution effect seen in λ4471. The velocity amplitudes required are comparable to those obtained in previous non-LTE studies of the metallic spectra of early-type supergiants, which lends support to the idea that the generalized dilution effect can be viewed as the 'microturbulence problem' in the He I ion (note that the effect is absent from OB dwarfs and giants which are characterized by low values of microturbulent velocity). We intend to examine that hypothesis by carrying out a star-by-star comparison of the microturbulent velocities obtained from applying the consistency criterion to He with those obtained via the conventional curve-of-growth analysis of CNO lines.

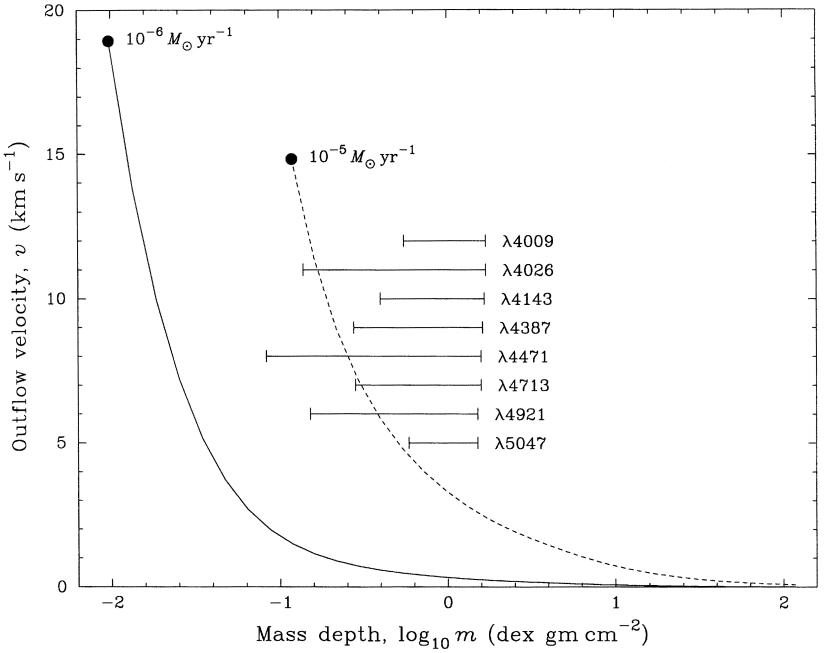

Figure 9. Predicted outflow velocity as a function of column mass below the sonic point (filled circles) in a hydrostatic atmosphere with parameters $T_{\rm eff} = 30\,$kK, $\log_{10} g = 2.9$ and $y = 0.09$. Velocity distributions obtained assuming mass-loss rates of $10^{-6}\,\mathrm{M}_\odot\,\mathrm{yr}^{-1}$ (solid curve) and $10^{-5}\,\mathrm{M}_\odot\,\mathrm{yr}^{-1}$ are compared. Horizontal bars indicate the mass depth range over which $\tau_\nu = 2/3$ in the profiles of several He I lines.

4.3 Microscopic or macroscopic velocity fields?

As we have demonstrated in this paper, the self-consistent introduction of microturbulence in line formation calculations offers a means by which the anomalous strength of triplet lines can be reconciled with those of singlets at near-solar helium number fractions. We have not addressed the origins of the putative velocity fields implicated in the microturbulent-like desaturation of He I lines identified here. Given that the required turbulent velocity amplitude is comparable to the photospheric isothermal sound speed, it is naturally preferable to look to non-stochastic fields as an explanation of the desaturation effect. Thinking along these lines, Kudritzki (1992) and more recently Lamers & Achmad (1994) have argued that the *macroscopic* velocity field in an expanding atmosphere can simulate microturbulence-like desaturation in metallic species such as iron. Although their calculations were based on the simple core–halo model comprising a supersonic wind matched to a subsonic hydrostatic photosphere, it is interesting to speculate whether the same mechanism might account for the He I desaturation effect that we have observed in O supergiants such as HD 152003. In the first instance it is necessary to establish that the expansion velocity gradient across the He I line formation zone is comparable to the microturbulent velocity amplitudes obtained here. This is difficult to do in the absence of an appropriate hydrodynamic model atmosphere, but a schematic calculation based on the hydrostatic case may be illustrative.

Following Kudritzki (1992) and Lamers & Achmad (1994), we assume that the density structure is well approximated by hydrostatic equilibrium below the sonic point (see Kudritzki 1988), which is defined as the location in the atmosphere at which the outflow velocity owing to mass loss is equal to the isothermal sound speed, namely

$$\dot{M}/4\pi R_\star^2 \rho_{\rm s} = \sqrt{kT_{\rm s}/\mu m_{\rm H}}, \qquad (6)$$

where $\dot{M}$ is the mass-loss rate, $R_\star$ is the stellar radius, $\rho_{\rm s}$ and $T_{\rm s}$ are the mass density and kinetic temperature at the sonic point, and μ is the number of atomic units per free particle. The subsonic velocity field then follows from the equation of continuity, $r^2 v\rho = r_{\rm s}^2 v_{\rm s}\rho_{\rm s}$, with the assumption that the radial coordinate is approximately constant – and equal to the radius at the sonic point – throughout the atmosphere (i.e. $r \simeq r_{\rm s}$). Adopting the best-fitting model parameters from Table 3 coupled with an assumed absolute visual magnitude of $M_V = -6.5$ yields a stellar radius for HD 152003 of $R_\star \simeq 30\,\mathrm{R}_\odot$. Using that estimate of $R_\star$ with a typical O9.7 Iab mass-loss rate of $\dot{M} = 10^{-6}\,\mathrm{M}_\odot\,\mathrm{yr}^{-1}$ (Howarth & Prinja 1989) gives the velocity distribution plotted as a function of column mass in Fig. 9 (solid curve). The depths of formation of several He I lines are indicated in Fig. 9 by horizontal bars, which correspond to the full range in column mass over which $\tau_\nu = 2/3$ through their profiles (that is, from line centre to continuum). It is clear from Fig. 9 that even the cores of the strongest lines are formed at outflow velocities of less than $2\,\mathrm{km\,s}^{-1}$ – considerably below the thermal velocity of helium. In fact, a mass-loss rate in excess of $10^{-5}\,\mathrm{M}_\odot\,\mathrm{yr}^{-1}$ is required in order that outflow velocities reach an appreciable amplitude in the line-forming zone (dashed curve in Fig. 9). Of course, this may be due to systematic errors in the T–ρ distribution of our model (for example, resulting from metal-line blanketing) or, more likely, a failure of the hydrostatic assumption below the sonic point. However, the inference from Herrero et al.'s (1995) analysis of HD 226868 is that relaxation of the hydrostatic assumption *alone* is unlikely to resolve the problem addressed in this paper. While that issue can only be resolved by further studies employing fully hydrodynamic models, it might nevertheless prove feasible to explore the impact of arbitrary subsonic macroscopic velocity fields on line formation in order to establish whether they are *in principle* capable of generating microturbulent-like desaturation in He I transitions.

5 CONCLUSIONS

We have shown that classical, isotropic microturbulence can play an important role in shaping the emergent flux profiles of certain saturated He I lines through interactions between bandwidth-related radiative transfer effects, perturbations of the populations of absorbing states, and changes in the gross atmospheric structure. In particular, we find that microturbulence exerts a *differential* impact on the strengths of singlet and triplet transitions of He I, which we have exploited in a non-LTE analysis of the late O supergiant HD 152003 in order to obtain excellent consistency between all diagnostically useful blue-region lines at a unique, near-solar value of y. We suggest that, by extension, microturbulence might prove useful (perhaps in conjunction with additional physics) in resolving the helium discrepancy and in explaining the generalized dilution effect, both of which are encountered when plane-parallel models are applied in the analysis of luminous OB stars. The microturbulent velocity that we infer by applying the 'consistency criterion' to He I lines in HD 152003 is comparable to the photospheric isothermal sound speed of the star, which naturally raises the question of the physical origin of the desaturating velocity field exposed by our analysis. We have shown that a suggestion made by previous authors – that the inferred microturbulence field is in fact an artefact of the neglect of atmospheric expansion owing to mass loss – cannot be confirmed using a simple core–halo model based on the parameters that we derive for HD 152003.

ACKNOWLEDGMENTS

We thank the referee, Keith Butler (USM), for his comments on the paper and in particular for his suggestion that we look at the influence of microturbulence on atmospheric structures. We are also grateful to both him and Ivan Hubeny (GSFC) for providing us with the latest versions of their codes and for ready advice in their implementation and use. Data reduction and analysis were carried out using hardware and software provided by the Starlink and CCP7 projects. The financial support of PPARC (grant GR/G41207) is gratefully acknowledged.

REFERENCES

Barnard A. J., Cooper J., Shamey L. J., 1969, A&A, 1, 28
Barnard A. J., Cooper J., Smith E. W., 1974, J. Quant. Spectrosc. Radiat. Transfer, 14, 1025
Bennet S. M., Griem H. R., 1971, Technical Report 71-097, University of Maryland, College Park, Maryland
Butler K., 1984, PhD thesis, University of London
Butler K., Giddings J. R., 1985, CCP7 Newsletter on Analysis of Astronomical Spectra No. 9, Daresbury Laboratory
Conti P. S., Ebbets D., 1977, ApJ, 213, 438
Gabler R., Gabler A., Kudritzki R.-P., Puls J., Pauldrach A., 1989, A&A, 226, 162
Giddings J. R., 1981, PhD thesis, University of London
Gies D. R., Lambert D. L., 1992, ApJ, 387, 673
Herrero A., 1993, Space Sci. Rev., 66, 137
Herrero A., Kudritzki R.-P., Vilchez J. M., Kunze D., Butler K., Haser S., 1992, A&A, 261, 209
Herrero A., Kudritzki R.-P., Gabler R., Vilchez J. M., Gabler A., 1995, A&A, 297, 556
Howarth I. D., Prinja R. K., 1989, ApJS, 69, 527
Howarth I. D., Siebert K. W., Hussain G. A. J., Prinja R. K., 1997, MNRAS, 284, 265
Hubeny I., Lanz T., 1995, ApJ, 439, 875
Kudritzki R.-P., 1976, A&A, 52, 11
Kudritzki R.-P., 1988, in Chmielewski Y., Lanz T., eds, 18th Advanced Saas-Fee Course, Radiation in Moving Gaseous Media. Geneva Observatory, p. 3
Kudritzki R.-P., 1992, A&A, 266, 395
Lamers H. J. G. L. M., Achmad L., 1994, A&A, 291, 856
Lennon D. J., 1994, Space Sci. Rev., 66, 127
Lennon D. J., Kudritzki R.-P., Becker S. R., Butler K., Eber F., Groth H. G., Kunze D., 1991, A&A, 252, 498
Lennon D. J., Dufton P. L., Fitzsimmons A., 1992, A&AS, 94, 569
Lennon D. J., Dufton P. L., Fitzsimmons A., 1993, A&AS, 97, 559
McErlean N. D., Lennon D. J., Dufton P. L., 1998, A&A, 329, 613
Mihalas D., 1978, Stellar Atmospheres, 2nd edn. W. H. Freeman & Co., San Francisco
Rauch K., Werner K., 1988, A&A, 202, 159
Schöning T., Butler K., 1989a, A&A, 219, 326
Schöning T., Butler K., 1989b, A&AS, 78, 51
Simon K. P., 1991, in Baade D., ed., ESO Proc. 36, ESO Workshop on Rapid Variability of OB-Stars: Nature & Diagnostic Value. ESO, Garching, p. 335
Smith K. C., 1997, in Lamers H. J. G. L. M., Nota A., eds, ASP Conf. Ser. Vol. 120, Luminous Blue Variables: Massive Stars in Transition. Astron. Soc. Pac., San Francisco, p. 208
Smith K. C., Howarth I. D., 1994, A&A, 290, 868
Smith K. C., Howarth I. D., Siebert K. W., 1998, in Howarth I. D., ed., ASP Conf. Ser. Vol. 131, Boulder–Munich II: Properties of Hot, Luminous Stars. Astron. Soc. Pac., San Francisco, p. 153
Voels S. A., Bohannan B., Abott D. C., Hummer D. G., 1989, ApJ, 340, 1073

This paper has been typeset from a TEX/LATEX file prepared by the author.